The grinding tip of the sea urchin tooth exhibits exquisite control over calcite crystal orientation and Mg distribution

Yurong Ma[a,1], Barbara Aichmayer[b], Oskar Paris[b], Peter Fratzl[b], Anders Meibom[c], Rebecca A. Metzler[d], Yael Politi[a], Lia Addadi[a,2], P. U. P. A. Gilbert[d,2,3], and Steve Weiner[a,2]

[a]Department of Structural Biology, Weizmann Institute of Science, Rehovot 76100, Israel; [b]Department of Biomaterials, Max Planck Institute of Colloids and Interfaces, 14424 Potsdam, Germany; [c]Laboratoire d'Etudes de la Matiére Extraterrestre, Centre National de la Recherche Scientifique NanoAnalyses 2679, Muséum National D'Histoire Naturelle, 75005 Paris, France; and [d]Department of Physics, University of Wisconsin, Madison, WI 53706

Edited by Jack Halpern, University of Chicago, Chicago, IL, and approved February 20, 2009 (received for review October 13, 2008)

The sea urchin tooth is a remarkable grinding tool. Even though the tooth is composed almost entirely of calcite, it is used to grind holes into a rocky substrate itself often composed of calcite. Here, we use 3 complementary high-resolution tools to probe aspects of the structure of the grinding tip: X-ray photoelectron emission spectromicroscopy (X-PEEM), X-ray microdiffraction, and NanoSIMS. We confirm that the needles and plates are aligned and show here that even the high Mg polycrystalline matrix constituents are aligned with the other 2 structural elements when imaged at 20-nm resolution. Furthermore, we show that the entire tooth is composed of 2 cooriented polycrystalline blocks that differ in their orientations by only a few degrees. A unique feature of the grinding tip is that the structural elements from each coaligned block interdigitate. This interdigitation may influence the fracture process by creating a corrugated grinding surface. We also show that the overall Mg content of the tooth structural elements increases toward the grinding tip. This probably contributes to the increasing hardness of the tooth from the periphery to the tip. Clearly the formation of the tooth, and the tooth tip in particular, is amazingly well controlled. The improved understanding of these structural features could lead to the design of better mechanical grinding and cutting tools.

echinoderms | grinding tool | self-sharpening | spectromicroscopy | X-ray microdiffraction

One of the most interesting paradigms in the field of biomineralization is the ability of the sea urchin tooth to grind down limestone, because both the tooth and the rock are composed almost entirely of calcite. This impressive ability is certainly related to the structure of the whole tooth and especially the organization of the materials that make up the mature end, that is, the grinding tip of the tooth. The sea urchin tooth has thus been studied extensively studied (1–10) to better understand the unique structural features that enable it to function so effectively as a grinding tool.

The major structural elements of the sea urchin tooth are primary plates and needles each of which is a single crystal of low Mg calcite (5–13 mol% Mg), and a Mg-enriched calcite polycrystalline matrix (40–45 mol% Mg), which is confined to the stone part of the tooth. The latter is the hardest part of the tooth and is located in its central part, when seen in cross-section (7). The primary plates and needles first form the framework of the sea urchin tooth, whereas the Mg-enriched polycrystalline matrix fills the spaces between the plates and the needles, during the later stages of tooth development. The Mg-rich polycrystalline phase has high hardness and elastic modulus values, and together with the plates and needles, is thought to play a key role in the grinding capability (11). The needles, plates, and polycrystalline matrix are all intimately associated at the micrometer-scale in the stone part of the tooth. The focus of this study is to better understand the structural organization of the tip by taking advantage of 3 highly resolving techniques that provide information on compositional variations and crystal orientations.

During tooth formation, a needle-plate complex forms a single crystal via an amorphous calcium carbonate (ACC) precursor phase (10). The needle-plate complexes have been described as being all aligned such that a whole tooth behaves as a single crystal (5, 12) based on X-ray diffraction, or as 2 crystals with a small angular offset based on polarized light microscopy (1–3); a dichotomy that is addressed in this study.

The needles and the plates are also known to have different material properties, even within a single crystal element. For example, the internal layer inside the plates is composed of ACC, and the cores of the needles are more soluble than their peripheries (7). The polycrystalline matrix crystals are so rich in Mg, that they were referred to as "protodolomite," because the structure corresponds to disordered Mg calcite (12). Wang et al. (7) showed that at least 75% of the Mg is located within the crystal lattice. They also noted that a membrane separates the needles from the polycrystalline matrix in the mature end of the tooth, and that within individual needles there is a gradient in the concentration of Mg.

In this study, we take advantage of the combination of several new experimental techniques that enable structures to be probed with spatial resolutions at different length scales ranging from nanometers to tens of micrometers. X-ray photoelectron emission spectromicroscopy (X-PEEM), combined with X-ray absorption near-edge structure (XANES) spectroscopy, provide structural (13), compositional (14), and orientational (15, 16) information. X-PEEM has a best resolution of 10 nm (17) (20 nm in this work) and a probing depth of a few nanometers (3 nm for carbon, 5 nm for oxygen, 12 nm for magnesium K-edges, and 3 nm for calcium L-edge) (16, 18). The recently developed polarization-dependent imaging contrast (PIC) displays with varying gray levels, different angles between the *c* axis of a carbonate crystal and the X-ray polarization vector (15, 16 19). Although the method is not quantitative, it can highlight and spatially resolve regions of cooriented or misaligned crystals (15, 16, 19,

Author contributions: Y.M., L.A., P.U.P.A.G., and S.W. designed research; Y.M., B.A., O.P., R.A.M., Y.P., and S.W. performed research; B.A., O.P., A.M., and P.U.P.A.G. contributed new reagents/analytic tools; Y.M., B.A., O.P., P.F., A.M., L.A., P.U.P.A.G., and S.W. analyzed data; and Y.M., B.A., O.P., L.A., P.U.P.A.G., and S.W. wrote the paper.

The authors declare no conflict of interest.

This article is a PNAS Direct Submission.

Freely available online through the PNAS open access option.

[1]Present address: Beijing National Laboratory for Molecular Sciences, College of Chemistry, Peking University, Beijing 100871, China

[2]To whom correspondence may be addressed. E-mail: lia.addadi@weizmann.ac.il, pupa@physics.wisc.edu, or steve.weiner@weizmann.ac.il.

[3]Previously publishing as Gelsomina De Stasio.

This article contains supporting information online at www.pnas.org/cgi/content/full/0810300106/DCSupplemental.

20). Microbeam X-ray diffraction can probe volumes in the micrometer regime (10-μm beam size in this work) to obtain local crystal orientation in 3-dimensions. A particularly powerful method is the combination of microbeam diffraction with scanning, that enables the production of 2-dimensional maps from the diffraction patterns (21, 22). In our case, information on the magnesium distribution can be determined from the dependence of the diffraction angle of Bragg reflections on the Mg concentration (23). The nano-scale secondary ion mass spectrometer (NanoSIMS) represents the latest generation of ion microprobes, which links high-resolution microscopy with isotopic analysis. The main advantage of NanoSIMS over other secondary ion mass spectrometers is its ability to operate at high mass resolution, while maintaining both excellent signal transmission and spatial resolution (down to 50 nm) (24–26). In this article, these 3 techniques are used to better understand the structure and organization of the crystals that make up the grinding tip of the sea urchin tooth.

Results

Both X-PEEM and X-ray microdiffraction provide information on the crystallographic alignments of the 3 structural elements in the tooth tip, and both provide information on the distribution of Mg in and around the tooth tip. The Mg distribution is also mapped using NanoSIMS.

Crystal Orientation. Fig. 1 *A–D* show 4 different X-PEEM maps from exactly the same cross-sectional area in the tooth tip. The low resolution Mg map (Fig. 1*A*) clearly shows the needles (elliptical dark spots) and plates (dark stripes) in the tooth tip. Needles and plates are both dark because they contain lower concentrations of Mg relative to the very high-Mg polycrystalline matrix (bright areas). Fig. 1*B* shows the Ca distribution map of the same region, where the needles and plates are brighter as they have higher Ca concentrations. Crystal *c* axis orientations were obtained from polarization-dependent imaging contrast (PIC) maps at the carbon and oxygen K-edges (Fig. 1 *C* and *D*, respectively). These maps were obtained by the digital ratio of X-PEEM micrographs, acquired at the π^* and σ^* peak energies for both carbon and oxygen. The C and O concentrations are the same in the different regions, because all of the stone part components are composed of Ca/Mg carbonate. The carbon and oxygen PIC maps are identical, because XANES spectra are sensitive to specific bonds, and C and O are bonded to each other in carbonates. The different gray levels in the carbon and oxygen PIC maps are thus due to different *c* axis orientations relative to the polarization vector in the illuminating X-ray beam (16) in alternating regions. Within each of these regions, not only are the tooth plates and needles aligned, but also the high Mg crystals that make up the polycrystalline matrix. Another interesting area is at the center of the stone part of the mature tooth. Here, too the carbon PIC map indicates 2 *c* axes orientations (Fig. S1). We note that the 2 orientations cannot be attributed to rotations in the *ab* plane, because X-PEEM PIC maps are insensitive to such rotations, although they are extremely sensitive to *c* axis rotations (see Fig. 2 in ref. 19). The needles and the polycrystalline matrix surrounding them have the same *c* axis orientations as they both have almost the same gray level (Fig. 1*F*). For reference the Mg map (Fig. 1*E*) is shown at the same magnification. These locally aligned and alternating regions have never been observed before in the sea urchin tooth. The X-PEEM PIC maps do not, however, provide quantitative information on the orientations of the 2 crystals, nor on the angular difference between the 2 *c* axis orientations (25).

We used microbeam X-ray diffraction to study the predominant orientations of calcite crystals in various parts of the tooth tip. Diffraction patterns were obtained from two 100-μm-thick transverse cross-sections (one of them is shown in Fig. 2*A*) and

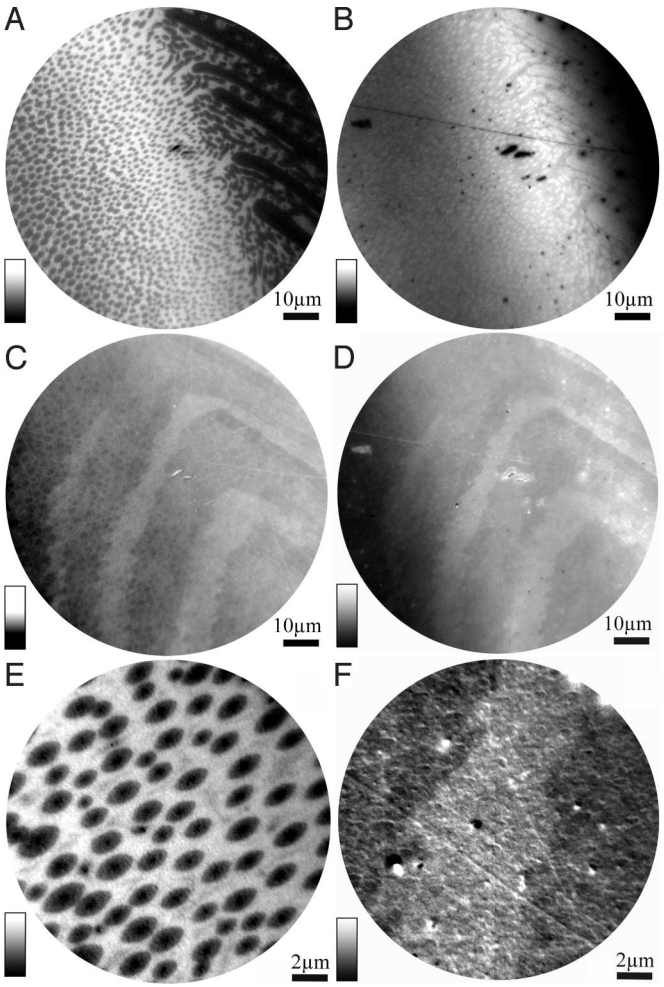

Fig. 1. X-PEEM elemental maps of the stone part in the transverse cross-section of the sea urchin tooth at the mature end, that is, the grinding tip of the tooth. (*A*, *B* and *E*) Elemental concentrations of Mg (*A*), Ca (*B*), and Mg (*E*). (*C*, *D*, and *F*) Carbon and oxygen polarization-dependent imaging contrast (PIC) maps, displaying different crystal *c* axis orientations with different gray levels. (*A–D*) Images are from the same area. (*E* and *F*) Images are from a small region in the center of the area shown in *A–D*. The pixel size in these maps is 100 nm for *A–D* and 20 nm for *E* and *F*. (*A*) Mg distribution map obtained by the digital ratio of images at 1302 eV and 1290 eV. These correspond to on-peak and pre-edge in Mg K-edge XANES spectra. In this and all other elemental maps, brighter gray levels indicate higher concentrations of the related elements. (*B*) Ca distribution map obtained by the digital ratio of images at 352.6 eV and 344 eV, on- and off-peak in Ca L-edge spectra. (*C*) Carbon PIC map obtained by digital ratio of 290.3 eV and 302 eV images, the π^* and σ^* peaks in carbon K-edge spectra from carbonates, respectively. Differences in gray level can only be attributed to different *c* axis orientations. Uniform gray levels indicate coaligned crystals. The image is darker on the left hand side, because of uneven illumination from the beamline. (*D*) Oxygen PIC map obtained by digital ratio of 534 eV and 540 eV images. Note that the carbon and oxygen PIC images are very similar, as expected. (*E*) Mg distribution map collected after zooming in on the central area of *A–D*. (*F*) Oxygen PIC map of the same region as in *E*, showing 2 distinct *c* axis orientations (two gray levels: darker on the left and right, lighter in the middle).

1 longitudinal section (Fig. S2), using a 10-μm-wide beam. Different positions on the tooth section were examined by rotating and oscillating the sample as described in the experimental section. Fig. 2*B* shows 1 quadrant of a 2D diffraction pattern obtained from the central region of the stone part for an oscillation angle of ± 90°. This "rotating crystal" diffraction pattern reveals essentially a single crystalline Mg-calcite pattern with a small (a few degrees) azimuthal spread of the reflections.

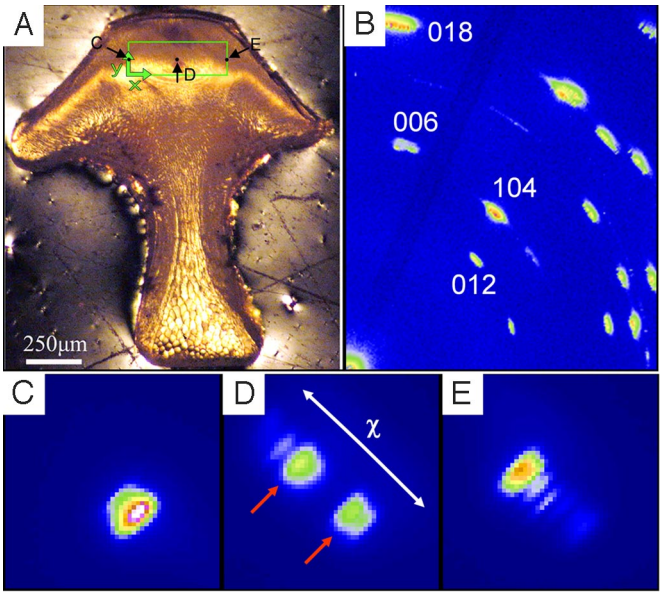

Fig. 2. Microbeam X-ray diffraction from a transverse cross-section in the stone part of the mature sea urchin tooth. The specimen thickness is ≈100 μm. The patterns were obtained at different rotation and oscillation angles around the vertical axis as a function of position with a beam size of 10 × 10 μm^2. The sample was oscillated by up to 90° to excite all reflections. (*A*) A polarized light micrograph of one typical specimen used for microbeam diffraction. The green box (360 μm × 150 μm) shows the region in the stone part where diffraction mesh scans were performed with a step size of 40 μm in the x (horizontal) and 30 μm in the y (vertical) direction starting from the lower left corner of the box. (*B*) Rotating crystal pattern (oscillation angle ± 90°) from the center of the green box shown in *A*. Some prominent calcite reflections are labeled. (*C–E*) Zoomed-in images of the (104) reflection of calcite obtained at positions y = 120 μm and x = 0 μm (*C*), x = 160 μm (*D*), and x = 360 μm (*E*), respectively, as indicated by arrows in *A*. All patterns correspond to a rotation angle of 2.5° with oscillation angle ± 7.5° (beam almost perpendicular to the cross-section). For the region close to the upper left corner (*C*) and the upper right corner (*E*) of the green box shown in *A*, only 1 prominent peak is observed. In the middle (*D*) there is a clear splitting into 2 strong reflections (arrows), which differ by 1.1° in azimuthal direction (the azimuthal coordinate χ of the 2D diffraction pattern is indicated). It should be noted that in addition to the strong peaks, several weaker (104) reflections with a maximum azimuthal spreading of ≈1.5° are also recognized in *D* and *E*.

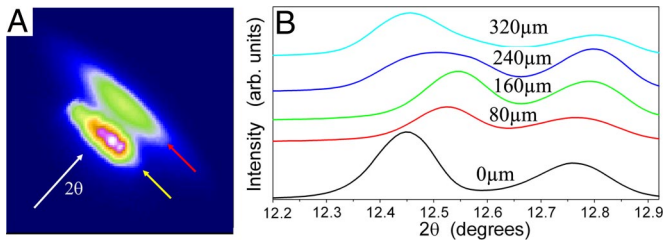

Fig. 3. Structural and chemical parameters derived from X-ray diffraction in the stone part within the box shown in Fig. 2*A*. (*A*) The 104 reflection measured close to the center of the green box in Fig. 2*A* (x = 160 μm, y = 60 μm). Two contributions are observed in the radial direction (scattering angle 2θ). The inner part (lower 2θ, indicated by the yellow arrow) corresponds to the Bragg peaks of the low Mg single crystals (mainly needles in this region), whereas the outer peak (higher 2θ, indicated by the red arrow) belongs to the high Mg polycrystalline matrix. (*B*) Radial diffraction intensity I(2θ) obtained by integrating the (104) diffraction peaks in the azimuthal (χ) direction. The profiles correspond to a horizontal line near the middle of the green box in Fig. 2*A* (vertical position y = 60 μm, horizontal positions as indicated). The mean peak positions were used to calculate and to map the Mg contents for the plate/needle complex and the polycrystalline matrix, and the relative amounts of the 2 phases, respectively (see Fig. S3).

The vertical symmetry line of the cross-section (corresponding to the rotation axis) is close to the [018] direction, and the calcite c axis (006) reflection is tilted by ≈15° with respect to the vertical.

The (104) reflection is shown in more detail for several positions in Fig. 2 *C–E*. Within the scanned region (green box in Fig. 2*A*), this reflection always appears in the rotation interval between −5° and +10°, where 0° corresponds to the beam being perpendicular to the cross-section. Two slightly different orientations are apparent in the pattern from the middle of the tooth tip (stone part) (Fig. 2*D*) as indicated by the presence of a double peak. However, on either side of the tooth stone part, only 1 peak dominates (Fig. 2 *C* and *E*). Similar observations were made for the entire upper region (60 μm from the top line of the green box in Fig. 2*A*), where plates and polycrystalline matrix dominate. In this region, the azimuthal angle varied by a maximum of 3°. In the lower part of the box in Fig. 2*A*, where needles dominate, a slightly broader distribution and typically >2 azimuthal maxima were observed (see the peaks indicated by the yellow arrow in Fig. 3*A*, as an example). Nonetheless, the profiles in this part of the tooth are generally consistent with the 2 main crystal orientations observed in the upper part. The azimuthal distribution of the polycrystalline matrix [appearing at a larger scattering angle 2θ because of its larger Mg-content (Fig. 3*A*)] generally follows the orientations of the needles and plates, but appears rather continuous and rarely shows separated peaks. We note that the X-PEEM images in Fig. 1 do show that the polycrystalline matrix has 2 alternating c axis orientations in the stone part of the sea urchin tooth.

An estimate for the upper limit of the tilt angle between the [104] directions in the central part of the tooth stone part is 5–10° (Fig. 2*D*). A more precise value cannot be determined from the present data as the specimen was oscillated by ±2.5°, and the reflections were typically observed within 2 successive rotation angles (increment 5°). We did note that the diffraction patterns from the longitudinal sections reveal essentially 2 single crystal Mg-calcite crystal patterns that are misoriented by ≈0.6° azimuthal difference based on the (006) reflection (Fig. S2). This indicates that, in this area, the two c axes are misoriented by less than ≈6° if we take into account the oscillation angle of ±2.5°. Note that this demonstrates that misalignments of 5° or less are clearly differentiated by the X-PEEM carbon and oxygen PIC maps.

Mapping of the Mg Concentrations. ***X-ray microdiffraction.*** The Bragg reflections are split in the radial (2θ) direction. Although the azimuthal intensity distribution is related to the crystal orientation, the radial splitting indicates changes in lattice spacing. These are most likely due to the difference in Mg concentrations between the needles/plates and the polycrystalline matrix (Fig. 3*A*). The inner peak (lower 2θ) corresponds to the needle/plate complex with a larger lattice spacing and the outer peak (higher 2θ) to the polycrystalline matrix with a smaller spacing because of a larger Mg content (5, 26). Fig. 3*B* shows the azimuthally integrated profiles of the (104) reflection along a horizontal line close to the middle of the green box in Fig. 2*A*. In most cases, 2 isolated peaks are visible. Both peaks shift with position, indicating gradients in Mg content of both the plate/needle complexes and the polycrystalline matrix, over a length scale of ≈40 μm. The radial position of the 2 peaks in Fig. 3*B* was used to determine the local Mg contents of the plate/needle complex and the polycrystalline matrix separately. A detailed mapping in the vertical direction shows an increase in both the Mg concentration and the relative amount of polycrystalline matrix from the periphery to the center of the stone part (Fig. S3).

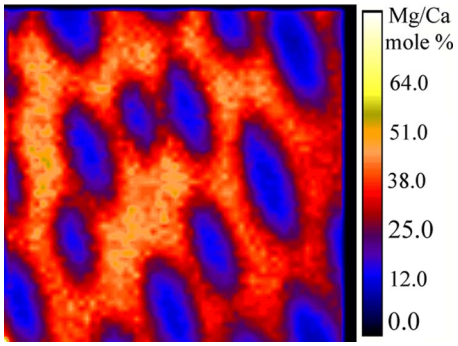

Fig. 4. Mg/Ca map of the transverse cross-section of the grinding tip of the sea urchin tooth, using NanoSIMS. Blue, low Mg calcite; red, high Mg calcite with Mg concentrations close to 45 mol%, i.e., compositionally similar to dolomite. The image is 5 mm across.

X-PEEM. X-PEEM provides information on Mg concentrations to a depth of ≈12 nm below the surface and at a much higher resolution (up to 20 nm) than microdiffraction (Fig. 1 *A* and *E*) (16). Although quantitative information on the local Mg concentration cannot be extracted, it is clear from Fig. 1 *A* and *E* that the Mg concentration is not uniform: the different gray levels show that the cores of the needles contain less Mg than their peripheries, and there are some low Mg zones within the polycrystalline matrix (Fig. 1*E*).

NanoSIMS. The NanoSIMS ion probe provides quantitative information on Mg concentrations at a resolution lower than X-PEEM, but much higher than the X-ray microdiffraction used here. The spatial resolution is ≈100 nm and the probing depth of each scan is ≈10 nm (23). Fig. 4 shows a Mg/Ca map of a polished transverse cross-section of the grinding tip. The Mg concentration of the polycrystalline matrix is close to that of dolomite, namely in the neighborhood of 45 mol% Mg, in agreement with the microdiffraction imaging of the Mg concentration of the polycrystalline matrix (Fig. S3). The Mg contents in the polycrystalline matrix are >3 times higher than those in the single crystalline needles (Fig. 4). Mg is distributed unevenly in the polycrystalline matrix, with areas of higher Mg contents being located at some distance from the needles. NanoSIMS shows that the cores of the needles have less Mg than their rims. Both of these observations are consistent with the X-PEEM results. Note that the size of the needles in Fig. 4 is larger than that of the needles in Fig. 1*E* because the area for the NanoSIMS analysis in Fig. 4 is farther away from the center of the stone part where the X-PEEM images in Fig. 1 were obtained.

Discussion

This high resolution structural and compositional study shows that in the sea urchin tooth tip the needles, plates and the high Mg polycrystalline matrix are all aligned. Furthermore, there are 2 differently-oriented crystalline blocks. The blocks are interdigitated in the stone part that is responsible for the grinding. The Mg concentrations in the tip are graded such that there is an overall increase in the Mg concentrations of both the needles and the polycrystalline matrix toward the center of the tip. The sea urchin tooth tip is clearly the product of exquisite control.

Ma et al. (10) showed that an individual plate-needle complex forms 1 single continuous crystal, despite its complex morphology. It is not known how many of these plate-needle complexes are aligned. One possibility is that all of the aligned components were actually only nucleated once, and that they are all part of 1 structural continuum. Because the tooth is composed of 2 such cooriented complexes, this would imply 2 slightly differently oriented nucleation sites.

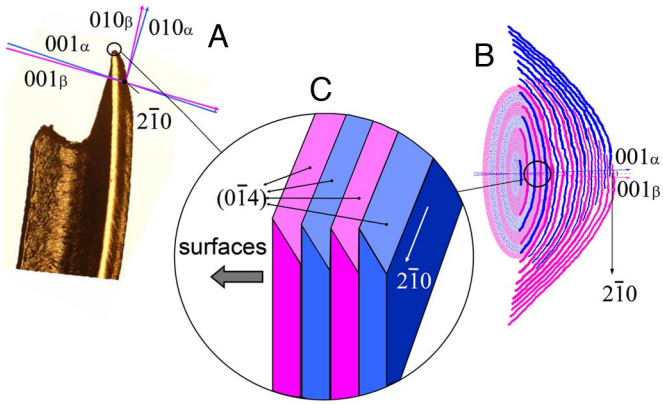

Fig. 5. Summary of crystallographic orientations of the calcite plates in the sea urchin tooth tip. (*A*) shows the approximate crystallographic orientations in relation in the tooth tip. (*B*) is a schematic illustration of the crystal orientations in the transverse cross-section of the sea urchin tooth at the mature end, near the grinding tip (viewed from the top). Each color represents a single crystal orientation, including cooriented single crystalline plates, needles and the polycrystalline matrix, collectively referred to as a crystalline ''block.'' Magenta and blue blocks alternate. Their calcite crystal c axes are separated at most by 1–6° and are both tilted off-plane by ≈15° from the vertical symmetry axis (as shown in *A*). The cross-section of the sea urchin tooth shows the 2 groups of primary plates on the 2 sides. The magenta and blue plates are drawn according to the SEM image of the transverse cross-section of the tooth shown in Fig. S4, where their structure is evident. At the center, the plates from one side are always covered by plates from the other side. The polycrystalline matrix aligned with the blue set of plates and needles is shown in pale blue, and the matrix aligned with the magenta set of plates and needles is in pale magenta. (*C*) An enlarged 3D schematic of the calcite plates in the tooth tip. The [2$\bar{1}$0] direction is perpendicular to the plane of observation in *A* and is indicated by an arrow in *B* and *C*. Cleavage planes (0$\bar{1}$4) (containing the [2$\bar{1}$0] direction) are terminating the plate edges near the grinding surface (*C*) of the calcite plates in the tooth tip.

The alignment of the nano-sized crystals of the polycrystalline matrix with the needles and plates is puzzling, because Wang et al. (7) reported the presence of a membrane of unknown composition around each needle in the tooth tip. The alignment is less puzzling if one assumes a process of secondary nucleation, starting from the plates, which are not coated by a membrane but by a loose network of organic molecules (7). In this scenario, crystal orientation would propagate through the network and eventually include all nanocrystals in the polycrystalline matrix. Furthermore, the extent of alignment of the crystals in the polycrystalline matrix is not as good as the alignment of the needles and the plates. This may indicate that the polycrystalline matrix constituents obtain their alignment by the mechanism of oriented attachment (27, 28), or by secondary nucleation upon contact.

We define a region of cooriented plates, needles, and the polycrystalline matrix as a ''block.'' The X-PEEM results show that only 2 kinds of blocks with different *c* axis orientations exist, as shown by the appearance of stripes with slightly different gray levels in PIC images. These stripes alternate regularly across the stone part of the mature sea urchin tooth, indicating that the two blocks are interdigitated. This is schematically illustrated in Fig. 5. X-ray microdiffraction basically confirms these observations, although 2 clearly defined orientations seem to be present only in the plate-rich regions of the tip, whereas, in the needle-rich regions, some intermediate orientations are also observed. Microbeam X-ray diffraction provides an estimate for the misalignment of the alternating blocks (Fig. S2). The misalignment is between 1° and 6° depending on the location. The presence of 2 crystals is consistent with the proposal of Märkel that the whole tooth has basically 2 orientations based on polarized light

microscope images (1–3). Polarized light microscopy images of thin sections of the tooth tips examined here (Fig. S5) are also consistent with Märkel's studies.

In this study, we show that the Mg contents increase from the periphery of the tooth tip to the center, in the plates and needles, and in the polycrystalline matrix. In addition, the relative proportion of polycrystalline matrix shows a strong gradient toward the grinding tip. We infer that this increase in Mg within the different structural elements, and the increase in the relative proportion of the polycrystalline matrix, both contribute to the mechanical design of the tooth as a grinding tool, following the studies of Wang et al. (7) and Ma et al. (11). Wang et al. (7) note that the Mg concentrations vary within a single needle, from ≈4.5 mol% in the keel to 13 mol% in the grinding tip. They also note that the dimensions of the needles decrease from 15–20 μm in the keel to ≈1 μm in the tip. These properties should also increase the hardness and stiffness of the needles in the tip.

It is interesting to consider the possibility that the presence of 2 slightly misaligned blocks and the fact that they are interdigitated in the grinding tip itself may have functional advantages. A detailed examination of the diffraction pattern presented in Fig. S2 shows the (006), the (012) and the (0$\bar{1}$4) diffraction spots. The zone axis in the diffraction pattern is perpendicular to the [2$\bar{1}$0] direction and contains the *a* axis. It also contains 1 variant of the cleavage plane for calcite, namely (0$\bar{1}$4). During grinding it can be expected that fracture will preferentially occur along the {104} cleavage planes. Fig. 5*C* schematically depicts these cleavage planes for the interdigitating plates of the tooth tip. Calcite plates derived from the 2 misaligned blocks are shown in different colours in Fig. 5*B*. The plates are slightly tilted around the [2$\bar{1}$0] direction. In each of the plates, (0$\bar{1}$4) cleavage planes form an edge with an angle close to 45° with respect to the grinding surface. The overall surface will thus be corrugated. As this surface wears down, the very small and relatively hard high Mg crystallites between plates would also be exposed in the grinding surface, as proposed by Ma et al. (11). Both properties could thus contribute to the grinding capability of the tooth tip. We also note that in this model, the edges of the individual plates would remain anatomically sharp due to cleavage along the {104} planes, and the cleavage would probably not propagate through the whole tooth tip because of the small misalignment between neighboring plates.

Conclusion

The mature sea urchin tooth possesses incredible structural and compositional complexity. Here, we show the presence of crystalline blocks composed of 3 different coaligned elements: needles, plates, and polycrystalline matrix. We also show that the tip, and presumably the whole tooth, is composed essentially of 2 such coaligned blocks that differ in their orientations by <6°. The blocks are also interdigitated in the tip. Furthermore, the Mg concentrations increase toward the center of the tooth tip. We propose that all of these features contribute to the grinding capability of the tooth. A deep understanding of the structural design features of the tooth tip sheds light on the manner in which one crystalline phase, calcite, can be tailored to fulfill grinding and self-sharpening functions that enable the tooth to be used to grind holes into a substrate that is also composed only of calcite. Much can be learned from the sea urchin tooth that can be applied to the development of improved grinding and cutting tools.

Materials and Methods

Cultured specimens of the Mediterranean echinoid *Paracentrotus lividus* were obtained live from the Israel Oceanographic and Limnological Research Company, Israel. The teeth were mechanically extracted from the Aristotle's lantern and were either processed immediately or were frozen at −70 °C for later use. Thin transverse cross-sections and longitudinal sections of sea urchin teeth with thicknesses of 100–200 μm were obtained by grinding and polishing the sample from both sides. Fresh sea urchin teeth were embedded in methyl methacrylate (Ultra-Mount; Buehler), and cured at room temperature overnight. The embedded samples were polished with a diamond suspension (DiaPro Dac, 3 μm, and DiaPro NAP B, 1 μm; Struers), and then an alumina suspension (AP-FF suspension, 0.1 μm; Struers) for the final polishing step. We analyzed 3 different teeth with X-PEEM, 3 with diffraction and 1 with nanoSIMS. Freshly bleached red algae (*Corallina elongata*, from the Mediterranean Sea), synthetic calcite (WARD'S Natural Science) and geological dolomite were also embedded and polished as described above.

X-PEEM and XANES. All samples for X-PEEM analysis were repolished with alumina grit down to 0.05 μm (Masterprep; Buehler), and coated with Pt to improve conductivity [1 nm of Pt in the analyzed area, 50 nm around it (29)]. X-PEEM and XANES spectra on the sea urchin tooth samples and controls were acquired at the Synchrotron Radiation Center (University of Wisconsin), using the SPHINX X-PEEM installed on the VLS-PGM undulator beamline (80–2,000 eV, spot size 100 μm × 300 μm, flux density up to 10^9 photons per μm^2·sec). The geometry of the SPHINX instrument was described by Frazer et al. (17). Briefly, the beam illuminates the sample at a grazing incidence angle of 16°, and the sample is mounted vertically, whereas the optics column is horizontal, and along the normal to the sample surface. The minimum detection limit for X-PEEM is on the order of 100 ppm to 1 ppt, depending on the specific absorption edge and its cross-section. In PIC maps, the only structures imaged are those with anticorrelated π^* and σ^* peaks at 290.3 and 302 eV, respectively. Both peaks and their anti-correlation are characteristic of carbonate groups, and both peaks are absent from any organic C spectra (16, 19).

Microbeam X-Ray Diffraction. Transverse cross-sections and longitudinal sections of the sea urchin tooth with a thickness of ≈100 μm were characterized by microbeam X-ray diffraction at the μ-Spot beamline at BESSY II in Berlin, Germany. The microbeam was defined by a toroidal mirror and a final pinhole of 10-μm diameter close to the sample, providing a beam size of approximately (10 × 10) μm^2 at the sample position. An energy of 19 keV (wavelength λ = 0.0652 nm) was selected by a Mo/BC multilayer monochromator. Two-dimensional diffraction patterns were collected in transmission mode, using a MARMosaic 225 CCD based area detector at a sample-detector distance of 283.9 mm. The beam center at the detector and the sample- detector distance were calibrated using a powder X-ray diffraction pattern of synthetic hydroxyapatite. The software Fit2D (A. Hammersley, European Synchrotron Radiation Facility, Grenoble, France) was used for data reduction and analysis.

The tooth sections were mounted on a *y*–*z* scanning table on top of a goniometer, with the possibility to rotate the sample around the vertical *z* axis. An on-axis optical microscope was used to determine the exact position on the sample before the examination by X-ray diffraction measurements. The goniometer rotation axis was adjusted such that the actual sample position hit by the X-ray beam was exactly in the intersection point of beam axis and the rotation axis. Thus, the X-ray spot remained at the same sample position, within the accuracy of ≈20 μm, during rotation of the sample. If the sample was rotated continuously during the collection of the diffraction pattern we denote this as "oscillation." X-ray diffraction patterns at different positions on the tooth sections were taken at different rotation and for different oscillation ranges in transmission mode. It should be noted that, for large rotation angles, the position resolution perpendicular to the rotation axis (i.e., in the horizontal plane) becomes strongly blurred because of the sample thickness of 100 μm.

Polarized Light Microscope. Transverse cross-sections of the sea urchin tooth at the mature end (grinding tip) with a thickness of 100 μm were characterized under polarized light and plain light, using polarized light microscopy (ECLIPSE E600W POL; Nikon).

NanoSIMS. Polished transverse cross-sections from the mature end of the sea urchin tooth were analyzed using nanoSIMS ion microprobe (Musèum National d'Histoire Naturelle, Paris). NanoSIMS analyses were carried out with a primary beam of negatively-charged oxygen focused to a spot-size of ≈100 nm on the surface of the sample. The secondary ions $^{24}Mg^+$ and $^{44}Ca^+$ were detected in multicollector mode with electron multipliers at a mass resolving power of ≈5,000, which allows all potentially problematic mass-interferences to be resolved (23, 24). Images of 256 by 256 pixels were obtained by rastering the primary beam across a presputtered surface with a pixel dwelling time of 10 ms.

ACKNOWLEDGMENTS. We thank Prof. Muki Spiegel, Sharon Marziano, and David Krugoliac from the Israel Oceanographic and Limnological Research

Company for providing fresh sea urchins; Chenghao Li, Stefan Siegel and Christoph Gilow for their help during the diffraction experiments carried out at the μ-Spot beamline at BESSY, Berlin, Germany; and Leslie Leiserowitz for useful discussions. This work was supported by the Minerva Foundation and the Helen and Milton A. Kimmelman Center for Biomolecular Structure and Assembly, Department of Energy Grant DE-FG02-07ER15899 (to P.U.P.A.G. and S.W.), and National Science Foundation Grant CHE&DMR-0613972 (to P.U.P.A.G.). The spectromicroscopy experiments were done at Synchrotron Radiation Center and supported by National Science Foundation award DMR-0537588.

1. Märkel K, Titschack H (1969) Morphology of sea-urchin teeth (in German). *Z. Morph Tiere* 64:179–200.
2. Märkel K (1970) The tooth skeleton of Echinometra mathaei (Blainville) (Echinodermata, Echinoidea). *Annot Zool Jap* 43:188–199.
3. Märkel K, Gorny P, Abraham K (1977) Microarchitecture of sea urchin teeth. *Fortschr Zool* 24:103–114.
4. Kniprath E (1974) Ultrastructure and growth of the sea urchin tooth. *Calcified Tissue Res* 14:211–228.
5. Stock SR, Barss J, Dahl T, Veis A, Almer JD (2002) X-ray absorption microtomography (microCT) and small beam diffraction mapping of sea urchin teeth. *J Struct Biol* 139:1–12.
6. Stock SR, Ignatiev KI, Dahl T, Veis A, DeCarlo F (2003) Three-dimentional microarchitecture of the plates (primary, scondary and carinar process) in the developing tooth of Lytechinus variegatus revealed by synchrotron X-ray absorption microtomography (micro CT). *J Struct Biol* 144:282–300.
7. Wang RZ, Addadi L, Weiner S (1997) Design strategies of sea-urchin teeth—Structure, composition and micromechanical relations to function. *Phil Trans R Soc London Ser B* 352:469–480.
8. Robach JS, Stock SR, Veis A (2005) Transmission electron microscopy characterization of macromolecular domain cavities and microstructure of single-crystal calcite tooth plates of the sea urchin Lytechinus variegatus. *J Struct Biol* 151:18–29.
9. Robach JS, Stock SR, Veis A (2006) Mapping of magnesium and of different protein fragments in sea urchin teeth via secondary ion mass spectroscopy. *J Struct Biol* 155:87–95.
10. Ma YR, Weiner S, Addadi L (2007) Mineral deposition and crystal growth in the continuously forming teeth of sea urchins. *Adv Funct Mater* 17:2693–2700.
11. Ma YR, Cohen S, Addadi L, Weiner S (2008) Sea urchin tooth design: An ''all-calcite'' polycrystalline reinforced fiber composite for grinding rocks. *Adv Mater* 20:1555–1559.
12. Schroeder JH, Dwornik EJ, Papike JJ (1969) Primary protodolomite in echinoid skeletons. *Geol Soc Am Bull* 80:1613–1616.
13. Stohr J (1992) *NEXAFS Spectroscopy* (Springer, Berlin).
14. Chan CS, et al. (2004) Microbial polysaccharides template assembly of nanocrystal fibers. *Science* 303:1656–1658.
15. Metzler RA, et al. (2007) Architecture of columnar nacre, and implications for its formation mechanism. *Phys Rev Lett* 98:268102.
16. Metzler RA, et al. (2008) Polarization-dependent imaging contrast in abalone shells. *Phys Rev B* 77:064110.
17. Frazer BH, Girasole M, Wiese LM, Franz T, De Stasio G (2004) Spectromicroscope for the PHotoelectron imaging of nanostructures with X-rays (SPHINX): Performance in biology, medicine and geology. *Ultramicroscopy* 99:87–94.
18. Frazer BH, Gilbert B, Sonderegger BR, De Stasio G (2003) The probing depth of total electron yield in the sub-keV range: TEY-XAS and X-PEEM. *Surf Sci* 537:161–167.
19. Gilbert P, et al. (2009) Gradual ordering in red abalone nacre. *J Am Chem Soc*, in press.
20. Zhou D, et al. (2008) Assignment of polarization-dependent peaks in carbon K-edge spectra from biogenic and geologic aragonite. *J Phys Chem B*, in press.
21. Paris O, et al. (2007) A new experimental station for simultaneous X-ray microbeam scanning for small- and wide-angle scattering and fluorescence at BESSY II. *J Appl Crystallogr* 40:S466–S470.
22. Paris O (2008) From diffraction to imaging: New avenues in studying hierarchical biological tissues with X-ray microbeams. *Biointerphases* 3:FB16–FB26.
23. Goldsmith JR, Heard HC (1961) Subsolidus phase relations in the system CaCO3-MgCO3. *J Geol* 69:45–74.
24. Herrmann AM, et al. (2007) Nano-scale secondary ion mass spectrometry—A new analytical tool in biogeochemistry and soil ecology: A review article. *Soil Biol Biochem* 39:1835–1850.
25. Meibom A, et al. (2008) Compositional variations at ultra-structure length scales in coral skeleton. *Geochim Cosmochim Ac* 72:1555–1569.
26. Meibom A, et al. (2004) Distribution of magnesium in coral skeleton. *Geophys Res Let* 31:L23306–L23310.
27. Penn RL, Banfield JF (1999) Morphology development and crystal growth in nanocrystalline aggregates under hydrothermal conditions: Insights from titania. *Geochim Cosmochim Ac* 63:1549–1557.
28. Xu AW, Ma YR, Cölfen H (2007) Biomimetic mineralization. *J Mater Chem* 17:415–449.
29. De Stasio G, Frazer B, Gilbert B, Richter K, Valley J (2003) Compensation of charging in X-PEEM: A successful test on mineral inclusions in 4.4 Ga old zircon. *Ultramicroscopy* 98:57–62.